Edinburgh Research Explorer

The structure of P21/c (Ca0.2Co0.8)CoSi2O6 pyroxene and the C2/c - P21/c phase transition in natural and synthetic Ca, Mg, Fe2+ pyroxenes

Citation for published version:
Tribaudino, M, Mantovani, L, Mezzadri, F, Calestani, G & Bromiley, G 2018, 'The structure of P21/c (Ca0.2Co0.8)CoSi2O6 pyroxene and the C2/c - P21/c phase transition in natural and synthetic Ca, Mg, Fe2+ pyroxenes' American Mineralogist. DOI: 10.1180/minmag.2017.081.036

Digital Object Identifier (DOI):
10.1180/minmag.2017.081.036

Link:
Link to publication record in Edinburgh Research Explorer

Document Version:
Peer reviewed version

Published In:
American Mineralogist

General rights
Copyright for the publications made accessible via the Edinburgh Research Explorer is retained by the author(s) and / or other copyright owners and it is a condition of accessing these publications that users recognise and abide by the legal requirements associated with these rights.

Take down policy
The University of Edinburgh has made every reasonable effort to ensure that Edinburgh Research Explorer content complies with UK legislation. If you believe that the public display of this file breaches copyright please contact openaccess@ed.ac.uk providing details, and we will remove access to the work immediately and investigate your claim.

Download date: 05. Apr. 2019

Revision #1

The structure of *P*2$_1$/*c* $(Ca_{0.2}Co_{0.8})CoSi_2O_6$ pyroxene and the *C*2/*c* - *P*2$_1$/*c* phase transition in natural and synthetic Ca, Mg, Fe^{2+} pyroxenes

Mario Tribaudino*[1], Luciana Mantovani[1], Francesco Mezzadri[1], Gianluca Calestani[1] and Geoffrey Bromiley[2]

[1]Dipartimento di Scienze Chimiche, della Vita e della Sostenibilità Ambientale, Parco Area delle Scienze 157/A, 43124 Parma, Italy
[2]School of GeoSciences, University of Edinburgh, Grant Institute, West Mains Road, Edinburgh EH9 3JW, U.K.

Abstract

The *P*2$_1$/*c* synthetic $(Ca_{0.2}Co_{0.8})CoSi_2O_6$ pyroxene was synthesized by slow cooling from melt at high pressure. Single crystals suitable for X-ray diffraction were obtained and refined. The results were compared to those of *C*2/*c* pyroxenes along the series $CaCoSi_2O_6$-$Co_2Si_2O_6$. Strong similarities in the crystal chemical mechanism of the transition with the synthetic $CaFeSi_2O_6$-$Fe_2Si_2O_6$ and $CaMgSi_2O_6$-$Mg_2Si_2O_6$ pyroxenes, both at an average and local level are apparent.

The results, examined together with two new refinements of pigeonite in the ureilites ALHA77257 and RKPA80239 and of a set of natural and synthetic *C*2/*c* and *P*2$_1$/*c* pyroxenes, show that the average cation radius in the M2 site is the driving force for the phase transition from *C*2/*c* to *P*2$_1$/*c* . The longest M2-O3 distances and the O3-O3-O3 angles follow the same trend, dictated only by the ionic radius in M2, in either synthetic or natural pyroxenes, regardless of the ionic radius of the M1 cations. The transition also affects the difference between bridging and non-bridging oxygen atoms and the extent of tetrahedral deformation, whereas the M1-O, M2-O1 and M2-O2 distances are unaffected by the transition and are determined only by the ionic radius of the bonding cation. The structural changes between the ionic radius and the high temperature *C*2/*c* and *P*2$_1$/*c* transitions are similar, and different from the high-pressure transition.

The analysis of natural and synthetic pyroxenes shows that the transition with composition occurs in strain free pyroxenes for a critical radius of 0.85 Å. Increasing strain stabilizes the *P*2$_1$/*c* structure to higher temperature and larger cation radius.

Finally, our results show that the monoclinic *P*2$_1$/*c* Ca-poor clinopyroxene, i.e the pigeonite mineral, crystallizes only at conditions where the structure is HT-*C*2/*c*, and changes to the *P*2$_1$/*c* symmetry during cooling.

Introduction

Quadrilateral pyroxenes are abundant and ubiquitous in nature. Their equilibria are the basis for petrological interpretations of mafic and ultramafic assemblages, and provide a thermometric constraint on the geological history of host rocks. As an example, two-pyroxene thermometry, based on the partitioning of Ca, Mg and Fe between coexisting quadrilateral clino and orthopyroxenes, is an established and widely used petrologic tool, (Lindsley 1983; Lindsley and Andersen, 1983). Quadrilateral pyroxenes are solid solutions of the end members diopside ($CaMgSi_2O_6$), enstatite ($Mg_2Si_2O_6$), hedenbergite ($CaFeSi_2O_6$) and ferrosilite ($Fe_2Si_2O_6$). Diopside and hedenbergite form complete solid solution in the monoclinic *C*2/*c* structure, while a large miscibility gap is present between the Ca-rich and the Ca-poor part of the quadrilateral. This gap is larger in Mg- than in Fe-rich compositions. Enstatite and ferrosilite also form a complete solid solution, making, together with a limited substitution with diopside and hedenbergite, the *Pbca* orthopyroxene family. In common practice, we refer to clino and orthopyroxenes as the *C*2/*c* and *Pbca* monoclinic and orthorhombic varieties, coexisting in several ultramafic rocks and meteorites. However, the picture would not be complete without consideration of the monoclinic $P2_1/c$ pyroxene, named pigeonite. Pigeonite is mainly found in igneous rocks that cooled rapidly, as an Fe-rich, Ca-poor phase. Natural pigeonites contain ~0.2 Ca atoms p.f.u, more than orthopyroxene, where the Ca content is less than 0.1 a.p.f.u.

Natural pigeonite is generally Fe-rich, but clinopyroxenes with Ca content at about 0.2 a.p.f.u. can be synthesized for any bulk Fe content. However, the synthesis of Mg-rich pigeonite requires high temperature-low pressure conditions seldom found in nature (Boyd and Schairer 1964; Lindsley and Andersen 1983; Tribaudino *et al.,*. 2002). Mg-rich pigeonite is found in meteorites, such as the achondrite family of ureilites, formed from cooling of an igneous assemblage at temperatures of about 1200-1300 °C (Takeda 1987; Tribaudino 2006).

There is a strong structural connection between *Pbca* and $P2_1/c$ pyroxenes, the former being a variety of the $P2_1/c$ phase, twinned at the unit cell scale: for this reason, the polyhedral bond distances in clino and orthoenstatite are very similar (Ohashi, 1984). However, the $P2_1/c$ structure is more flexible than the *Pbca* structure and can host larger cations such as

Ca in the M2 site. This explains the structural changes observed when Mg and Fe substitute for Ca. Ca-rich pyroxenes, where the M2 site is most filled by Ca, have a *C*2/*c* space group; with decreasing Ca content, a transition to the $P2_1/c$ structure occurs. In only almost Ca-free pyroxenes, the orthopyroxene structure is formed. Recently, the high-pressure transition of orthopyroxene to a $P2_1/c$ pyroxene has additionally been reported (Zhang *et al.,* 2013, 2014).

In natural pyroxenes, a wide miscibility gap between clino and orthopyroxenes hides the $C2/c$-$P2_1/c$-*Pbca* sequence, which can be studied in samples synthesized from subsolidus. In (Ca,Mg)$MgSi_2O_6$ pyroxenes extended solid solution is possible only at very high temperatures (>1450°C), and during quenching exsolution textures are easily formed (Tribaudino *et al.,*. 2002; Weinbruch *et al.,* 2003), whereas in (Ca,Fe)$FeSi_2O_6$ and (Ca,Co)$CoSi_2O_6$ pyroxenes the synthesis can be performed successfully at lower temperature, and provides homogenous crystals.

Structural changes at the transition between *C*2/*c* and $P2_1/c$ have been described for (Ca,Fe)$FeSi_2O_6$ synthetic pyroxenes (Ohashi *et al.,*1975) whereas in (Ca,Mg)$MgSi_2O_6$ pyroxenes the transition could be only pinpointed by TEM (Tribaudino, 2000). The same phase transition was studied in $LiM^{3+}Si_2O_6$ pyroxenes with M^{3+} = M1 site = Al, Ga, V, Fe, Sc and In) in Redhammer et al. (2004), and in $LiFeGe_2O_6$ pyroxene by Redhammer et al. (2010). Results on synthetic samples provided a wealth of information on the general issue of the structural changes occurring as Ca is exchanged by a smaller cation, but, as yet, no effort has been made to apply the results to some natural cases.

Recently, a series of (Ca,Co)$CoSi_2O_6$ (hereafter Ca-Co) pyroxenes was synthesized, showing evidence of a phase transition at the composition of 0.4 a.p.f.u. (Mantovani *et al.,* 2014); the *C*2/*c* Ca-rich samples of the series were studied by single crystal refinement in Mantovani *et al.* (2013). Cobalt, as Co^{2+}, is a minor element in the composition of natural pyroxenes. However, it is interesting as it provides a synthetic model for natural pigeonite: the Co^{2+} ionic radius (0.745 Å), intermediate between that of Fe^{2+} (0.78 Å) and Mg^{2+}(0.72Å), is quite close to the average M1 cation radius of natural pigeonite .

In this paper the refinement of a $P2_1/c$ pyroxene with composition $(Ca_{0.2}Co_{0.8})CoSi_2O_6$ is reported, together with results of the refinement of pigeonite in two ureilites, with a high Mg content and an average ionic radius in the M2 site lower than in most $P2_1/c$ pyroxenes. The aim is to integrate results on the (Ca,Co)$CoSi_2O_6$ pyroxenes with literature refinements on synthetic and natural pigeonite and to discuss the general issue of structural changes occurring through the transition between Ca-rich and Ca-poor pyroxenes.

Experimental

A synthetic pyroxene with composition $(Ca_{0.2}Co_{0.8})CoSi_2O_6$, and two natural pigeonites picked from the ALHA77257 and RKPA80239 ureilites were refined. The ureilitic pyroxenes were previously characterized by TEM and SEM-EDS analysis (Tribaudino, 2006).

Synthesis of the Co-bearing pyroxene

Our Ca-Co pyroxene was synthesized at a pressure of 3 GPa, as at lower pressure olivine and a silica phase are stable instead of pyroxene. After annealing at room temperature, starting material with bulk composition $(Ca_{0.2}Co_{0.8})CoSi_2O_6$ was put in a 5 mm inner diameter, 10 mm long, Pt capsule with 20 wt% distilled water to aid crystal growth, and welded shut. The experiment was run in a 0.5 inch graphite-talc-pyrex piston-cylinder assembly; the sample was first pressurised, heated at 1500 °C for 30 min, slowly cooled from 1500 to 1350 °C, and eventually annealed for 6 h at 1350°C. Temperature was measured with a $Pt\text{-}Pt_{10}\%Rh$ thermocouple. Further experimental details are reported in Mantovani *et al.* (2013). Single crystals of Co-pyroxene crystals, with sizes up to 75-100 μm, were obtained, among which those examined for single-crystal XRD were selected for sharp optical extinction. No glass was found after the synthesis. XRD powder diffraction and SEM-EDS characterization confirmed that pyroxene and quartz (due to the excess of SiO_2 in the starting material) are the only phases.

TEM and SEM-EDS analysis

SEM-EDS analysis was done on polished grains after embedding in epoxy, following the same analytical procedures as in Mantovani *et al.* (2013). No deviation from the nominal stoichiometry was observed in the $(Ca_{0.2}Co_{0.8})CoSi_2O_6$ pyroxene; the two ureilitic pigeonites were analysed in Tribaudino (2006), and have compositions of $Ca_{0.12}Mg_{1.54}Fe_{0.24}Mn_{0.02}Cr_{0.03}Al_{0.03}Si_{2.00}$ and $Ca_{0.12}Mg_{1.54}Fe_{0.29}Mn_{0.01}Cr_{0.03}Al_{0.03}Si_{1.98}$ for ALHA77257 and RKPA80239 respectively.

TEM characterization was reported in previous papers (Tribaudino, 2006; Mantovani *et al.,* 2014). The two ureilitic pyroxenes show stacking disorder along the a* axis, likely related to a shock imprinting, but no exsolution textures, such as spinodal decomposition or augite lamellae. Streaking is also observed along the a* axis in SAED patterns from the Co pigeonite, indicative of some stacking disorder, but again, there is no evidence of exsolution textures (Mantovani *et al.,* 2014).

Single crystal X-ray diffraction

The crystals for single crystal X-ray diffraction were chosen carefully, as they proved highly defective. Several grains, chosen for their sharp optical extinction, showed diffractometer peak enlargement and peak splitting.

The single crystal data collection was performed on the $(Ca_{0.2}Co_{0.8})CoSi_2O_6$ pyroxene with a Bruker Smart device, equipped with an Apex II CCD detector using MoKα radiation. The full reflection sphere was measured up to $2\theta_{max} = 64°$. Due to partial superimposition of the reflections induced by the presence of twinning, the data reduction was performed with the TWINABS program (Sheldrick, 2009). The refinement was then carried out by using the HKLF 5 command of SHELXL-97 (Sheldrick, 1997), allowing to properly determine the intensity contribution to the common reflections after assignment of the scale factor to each twin individual. Consequently no R(int) is provided for this composition. For the two ureilitic pyroxenes a four circle diffractometer was used, and the same experimental conditions described for the refinement of the Y-791538 pigeonite in Tribaudino (2006), i.e. θ-2θ scan, using graphite monochromatizer Mo*Kα* radiation (λ=0.71073); a correction for absorption using the ψ-scan method was done, but did not improve the results and was therefore discarded. The intensity data were corrected for absorption by the SADABS program (Sheldrick, 1996), and the *P*2₁/*c* space group was confirmed by an analysis of the reflection extinctions. Weighted structural anisotropic refinements were performed using the SHELXL-97 program (Sheldrick, 1997), within the WinGX suite (Farrugia, 1999). The refinement was performed in the *P*2₁/*c* structure starting from the coordinates of the synthetic $Ca_{0.15}Mg_{1.85}Si_2O_6$ pigeonite (Tribaudino *et al.,* 2003). In the $(Ca_{0.2}Co_{0.8})CoSi_2O_6$ pyroxene, the M2 site was filled by Ca and Co, whereas full site occupancy of Co and Si were assumed for the M1 and T sites. In the ureilitic pyroxenes, Ca was fixed in the M2 site, Al and Cr in the M1 site, with the occupancy obtained from EDS analysis. The occupancies of Fe and Mg were refined in the M2 and M1 structural sites, within constraints of the determined chemical composition. Lastly, Mn was partitioned between the M1 and M2 sites as in Pasqual *et al.* (2000).

Anisotropic refinement was allowed, with all positive definite ADP's. Difference Fourier maps did not show residuals higher than $1e^-/Å^3$ for any of the samples.

Cell parameters and main structural results, fractional coordinates and displacement parameters, selected bond length and angles are reported in Tables 1, 2, 3 and 4.

Results

Average structure

The average structure of the $Ca_{0.2}Co_{1.8}Si_2O_6$ pyroxene is discussed here together with that of other Ca-Co pyroxenes. The trend observed in the simplified system provides insight into the subsequent discussion of natural pigeonites (Figs. 1 and 2)

Among the refined Ca-Co pyroxenes, $Ca_{0.2}Co_{1.8}Si_2O_6$ is the only one exhibiting $P2_1/c$ symmetry, and has the lower Ca content. Between $(Ca_{0.4}Co_{0.6})CoSi_2O_6$ and $(Ca_{0.2}Co_{0.8})CoSi_2O_6$ there is a phase transition from $C2/c$ to $P2_1/c$, with loss of lattice centering due to differential kinking of the formerly unique tetrahedral chains. One, the B chain, undergoes further kinking, whereas the other, the A chain, is released, and rotates in the opposite direction. The result is that the A chain is elongated, and kinked opposite to the B chain (S rotation) (Fig. 1). The chain rotation at the transition is dramatic: in Co pyroxenes the progressive substitution of 0.6 Co atoms for Ca in M2 between $CaCoSi_2O_6$ and $(Ca_{0.4}Co_{0.6})CoSi_2O_6$, decreases the kinking angle by only 3°, whereas a further substitution of 0.2 Co between $(Ca_{0.4}Co_{0.6})CoSi_2O_6$ and $(Ca_{0.2}Co_{0.8})CoSi_2O_6$ rotates the A and B chains by 25° and 17°, respectively. These values are similar for Ca-Fe and Ca-Mg pyroxenes and are related to the phase transition at a critical average ionic radius in the M2 site. M2-O3 bond distances are affected consequently.

In contrast, tetrahedral chain rotation has minor influence on the M2-O1 and M2-O2 bond distances, which deviate from the trend observed in $C2/c$ Co-pyroxenes only by a minor split in formerly equivalent distances. In $(Ca_{0.2}Co_{0.8})CoSi_2O_6$, the difference between the split distances in the $P2_1/c$ structures, as measured from the splitting of the $C2/c$ M2-O3C2,D2 and M2-O3C1D1 couples, is 0.85 and 0.56 Å, whereas the split of the M2-O2 and M2-O1 is just 0.02 and 0.03 Å, respectively (Figs. 2 and 3).

In the M1 polyhedron the bond distances in the Ca-poorer part of the join with $P2_1/c$ symmetry are consistent with those of Ca-richer $C2/c$ (Fig. 2). Again, limited splitting in the M1-O octahedral distances occurs, between 0.02 and 0.03 Å (Fig. 3b). On average, the M1-O bond distances change very little along the series, in agreement with the common presence of Co in the M1 site.

The transition also affects the tetrahedral configurations. T-O1, T-O2 and the two T-O3 bond distances, unique in *C*2/*c*, split in the *P*2_1/*c* symmetry, with different values in each of the tetrahedral chains (Fig.2). The tetrahedra in the A and B chains have significantly different configurations: the average bond distances are longer in the B chain of the tetrahedra (Fig. 2), and the difference between bond lengths for bridging and non-bridging oxygens is also larger (Fig. 3a). In the *C*2/*c* structure the difference between the average T-O of the two shorter non-bridging and the two T-O longer bridging distances decreases as the longer M2-O3 distances increases. In the *P*2_1/*c* pyroxene the difference between average T-O bridging and non-bridging in the B chain increases, compared to the last *C*2/*c* $(Ca_{0.4}Co_{0.6})CoSi_2O_6$, whereas in the A chain it decreases somewhat (Fig.3a). In *P*2_1/c, a higher bond angle variance is found in the A tetrahedron, whereas the distortion in the B tetrahedron follows the *C*2/*c* pyroxene trend (Fig.3c). The larger distortion of the A chain is related to the lower value of the O3A-Si-O3A angle with respect to the ideal tetrahedron (106.2° *vs* 109.5°); while the O3B-Si-O3B is closer to the ideal value (110.5°). This is an effect of the higher value of the kinking angle in the A chain (Fig. 2b). The A chain, which is significantly more elongated than the B chain, should be longer, but for symmetry, the Si_2O_6 unit repeat along the c axis must be the same in both chains. This is achieved by intra-tetrahedral deformation: the distance between the O3-O3 atoms in the A tetrahedron is smaller (2.630 vs 2.728 Å in the A and B chains respectively), and the O3A-Si-O3A angle is smaller than the corresponding O3B-Si-O3B (Fig. 3b).

Local structure

Larger atomic displacement parameters (ADP's) are found in $P2_1/c$ pigeonite with respect to Ca-free clino and orthopyroxenes (Ohashi *et al.,* 1975, Ohashi and Finger, 1976, Tribaudino *et al.,* 2003).

The large displacement parameters are related to the local deformation inherent in the substitution of Ca for a smaller cation, which promotes a local configuration for Ca sites. A split configuration for the M2 cations and some oxygen has been refined in $P2_1/c$ pyroxenes $Ca_{0.15}Mg_{1.85}Si_2O_6$ and $Ca_{0.23}Mg_{1.77}Si_2O_6$ (Tribaudino and Nestola 2002).

In $Ca_{0.2}Co_{1.8}Si_2O_6$ a split refinement failed to find consistent minima for the split configuration, with unrealistic short Ca-O 1.9 Å bond distances. We interpret this as the result of lower crystal quality, which biased the resolution, but also for the higher scattering power of Co than Mg, which masks the scattering contribution of Ca. However, there is evidence of local configurations in the Co pyroxene, comparing the size and orientation of the displacement parameters with those in clinoenstatite and in $Ca_{0.15}Mg_{1.85}Si_2O_6$ (Fig. 4 and tab. 4). The size of the displacement parameters is larger in the Ca-Co pyroxene, but the orientation of the ADP's in Ca-Co pyroxene is similar to that of the Ca bearing $Ca_{0.15}Mg_{1.85}Si_2O_6$, and different to clinoenstatite. In Ca bearing $P2_1/c$ pyroxenes the orientation of the M2 and O3 ADP's is almost parallel to the diad axis (i.e. normal to the c axis projection), whereas that of the O2b is along the M2-O2 bond. In clinoenstatite the orientation of the oxygen ADPs is normal to the M2-O bonding, and the longer axes of the ADP's of the M2 lie in the (010) plane.

In Fig 5 we show the size of the major axis of the displacement parameters of oxygen as a function of Ca content. In clinoenstatite the oxygens all have the same length, which may be interpreted as solely due to thermal vibration. With increasing departure from the end member the displacement ellipsoid of oxygen becomes larger, and to an extent different for the different oxygens. The O2b, O3a and O3b show a larger increase with Ca content. A split configuration for these oxygens is then suggested. For the O3 oxygen the larger ADPs are related to the coexistence of Ca rich and Ca poor local environments, as O3 is most involved in the transformation from Ca-rich and Ca-poor pyroxenes. Local Ca environment has a tendency to retain the *C*2/*c* local symmetry, and it is not surprising that the O3 oxygen show the highest local disorder. O2 is an under-bonded oxygen in pyroxenes (Cameron and Papike 1981), and also shows, with Ca substitution, higher displacement throughout the *C*2/*c* series (Ohashi *et al.,* 1975, Mantovani *et al.,* 2013). Among the O2a and b sites, it is O2b is which shows a higher change in bond distances across the transition.

Discussion

Structural changes in natural and synthetic pigeonite: the role of the ionic radius

The exchange of Mg, Co and Fe for Ca in the M2 site of quadrilateral and Co pyroxenes shares several common features:

1) there is a $P2_1/c$- $C2/c$ phase transition driven by differential kinking of the tetrahedral chains, ascribed to the decreasing size of the M2 cation;

2) in the $C2/c$ symmetry the cell volume is mostly dependent on the size of the M2 cation, whereas at the transition an excess negative volume is found (Mantovani *et al.,*. 2014);

3) the volume of the M1 polyhedron, which is occupied only by Co, Mg and Fe, is almost unchanged with Ca content;

4) there are other minor common structural features: a decreased difference between the tetrahedral distances, a split in the M2 polyhedron in M2 and M2' two subsites and a very similar cell deformation (Ohashi *et al.,*. 1975, Tribaudino *et al.,*. 1989; Mantovani *et al.,* 2013, 2014).

These changes are related to variation of the cation radius in a polyhedron where the M2-O bonding is mostly ionic in character (Cameron *et al.,*. 1973; Cameron and Papike, 1981).

In Zn pyroxenes along the $CaZnSi_2O_6$-$Zn_2Si_2O_6$ series the above listed changes do not occur, in spite of the very similar cation size of Zn and Co: the $C2/c$ -$P2_1/c$ transition is not observed, the cell volume does not depend on the M2 cation size and the M1 polyhedral volume changes significantly with composition. Only the M2-M2' split is found, but Zn lies in a position different from that occupied by Fe, Mg and Co. This is a consequence of the preference of Zn in the M2 site for covalent bonding, in contrast to the largely ionic behaviour of Mg, Fe and Co in the M2 site (Gori *et al.,*. 2015).

The above observations can be extended to the analysis of natural pigeonites. The main problem in the application of the results of synthetic samples to natural ones is the poor constraint that we have on chemical composition, due to extended solid solutions. In natural pigeonite a mixed occupancy in the M2 and M1 sites is found, with an M2 site filled by Ca, Na, Mg, Fe, Mn and the M1 by Mg, Fe, Ti, Al, Cr (Pasqual *et al.,* 2000).

To cope with the problem of mixed occupancy we compared crystals with different composition by calculating the average ionic radius in the M2 site. The M2 polyhedron is rather flexible, and it can deform to host a cation in eightfold or in six-fold coordination, depending on the ionic radius. As discussed by Downs (2003), when the M2 site is occupied by Ca, its coordination is eightfold, but it becomes six-fold coordinated if Mg, Fe or Co are present. In the eightfold coordination the M2 cation lies along the diad axis, in the $C2/c$ symmetry, whereas in the six-fold it is off the axis, prompting for a $P2_1/c$ symmetry. Downs (2003) showed that this off-the-axis transformation reduces M2-Si repulsion. In natural or synthetic pyroxenes with mixed M2 occupancy, the exchange of a smaller for a larger cation switches the M2 cation to a six-fold coordination, which is not supported by a *C*-centered lattice. The transition to the $P2_1/c$ structure was pinpointed at an M2 cation radius between 0.86 and 0.89 Å (Arlt and Angel 2000; Alvaro *et al.,*. 2010; Mantovani *et al.,*. 2014).

A selection of refinements on natural pigeonite was used to discuss the relations between natural and synthetic pyroxenes, discarding those where exsolved augite coexists with the pigeonite (e.g. sample BTS302 in Tribaudino *et al.,*. 2003). For this purpose, the two newly refined ureilitic pyroxenes were added to the database of natural pigeonite. The average M2 cation radius was calculated from the published site occupancies, and related to the O3-O3-O3 kinking angle (Fig. 6). The kinking angle is most unaffected by the M1 polyhedron as the O3 atoms are only linked to the M2 site and to the tetrahedral chain.

From the O3-O3-O3 kinking angle an indication of a transition at ~0.85Å is apparent. The transition can be well determined by crystal structure analysis of homogeneous crystals in Ca-Co and Ca-Fe at ~0.85Å (Ohashi *et al.,* 1975; Mantovani *et al.,* 2013).

A trend dictated only by ionic radius of the M2 cation is found also in the other M2-O bond distances, with the exception of the shorter M2-O3 distances, which are affected also by the cation in the M1 site (Fig 7).

In the M1 polyhedron the average ionic radius of the M1 site and the M1-O average distances are linearly related (Fig. 8). Differences in the M1-O average bond lengths due to the different cation substitutions in the M2 site are present, as a steric effect (Ghose *et al.,*. 1987), but are trivial respect to the contribution of the cation size.

In contrast, the tetrahedral distances show a marked effect with the transition. In the *C*2/*c* pyroxenes the difference between the T-O3 bridging and non-bridging T-O1, T-O2 distances shows a linear decrease with the M2 ionic radius. As the difference between <T-O_{br}> and <T-O_{nbr}> oxygen decreases to the value of 0.03 Å, a turnover is observed, with the transition to the $P2_1/c$ symmetry. In the $P2_1/c$ symmetry, the difference between the four bridging and non-bridging distances increases. The *C*2/*c* trend is instead observed in Ca-poor Zn-pyroxenes, where the phase transition is not observed (Fig.9).

The $P2_1/c$-C2/c phase transition with composition, temperature and pressure

In the previous paragraph we showed that in synthetic and natural pigeonite the kinking O3-O3-O3 angle is related to the ionic radius of different chemical species occupying the M2 site, with little inference on what is present in the M1 site (Fig. 6). As the opposite kinking of the tetrahedral chains is the driving force for the phase transition to the $P2_1/c$ structure (Alvaro *et al.,*. 2010) we may take the difference in the kinking angle between the two symmetry independent chains in the $P2_1/c$ structure as an order parameter of the phase transition. This is comparable to the well-known tilting behaviour in perovskites, which display Φ octahedral angle tilting as an order parameter (Lufaso and Woodward, 2004).

The difference O3-O3-O3 kinking angle probes the transition irrespective of the physical process driving the structural change: the mechanism is the same, i.e. a change in the kinking angles and a rearrangement of the tetrahedral chains, regardless of whether we consider increasing temperature, decreasing pressure or increasing ionic radius. However, approaching the transition the difference in kinking angles increases with pressure and decreases with temperature: as shown in Fig. 7 the pre-transition behaviour of the tetrahedral chains in the $P2_1/c$ phase at high pressure is opposite to that at high temperature. Also, the intensity of the *h*+*k* odd reflections, present in the $P2_1/c$ but not in the $C2/c$ symmetry, increases with pressure, i.e. approaching the phase transition (Nestola *et al.,*. 2004, Alvaro *et al.,*. 2010).

The different behaviour at high pressure and high temperature is apparent in Fig. 10, where the difference in the O3-O3-O3 kinking angles is plotted *vs* the longest M2-O3A distance, which is out of coordination in $P2_1/c$ pyroxenes. At high-pressure, the difference in tetrahedral chains increases, but the longest bond distance decreases, whereas at high temperature both decrease. Compositional changes follow a path very close to that at high temperature, indicating a similar structural trend between the high temperature and compositional driven transitions.

The $P2_1/c$-$C2/c$ phase transition: the role of strain

The related HT and compositional behaviour provides a clue to explain the difference between the single crystal X-ray observations that the critical ionic radius of the M2 cation for the transition in Ca-Co and Ca-Fe pyroxenes is about 0.85 Å (Ohashi *et al.,* 1975; Mantovani *et al.,* 2013, 2014), and TEM observations which indicate that the transition occurs at 0.89Å in Ca-Mg pyroxenes (Tribaudino, 2000; Arlt *et al.,*. 2001; Alvaro 2010). The difference is surprising, as the structural trend with the O3-O3-O3 and ionic radius is very similar, regardless of whether Ca is exchanged by Fe, Co or Mg (Fig. 6). TEM investigation have shown that intermediate Ca-Mg pyroxenes, due to the higher temperature of the solvus, show a mottled texture formed during cooling. The textures are preliminary to spinodal decomposition, and are indicative of local clustering. As an effect, the crystals are highly strained, already at high temperature. The effect of this strain was explored by Tribaudino *et al.* (2002) in a single crystal investigation of the $P2_1/c$-$C2/c$ transition at high temperature in $Ca_{0.15}Mg_{1.85}Si_2O_6$. The formation of strain modulations in a formerly homogeneous $Ca_{0.15}Mg_{1.85}Si_2O_6$ crystal during heating in an in situ experiment at 1200°C increased by more than 200°C the transition temperature with respect to that in the unstrained crystal. However, it should be noted that the evolution of the unit cell parameters is almost the same in strained and unstrained samples. In view of the similarity between high temperature and composition driven transitions, the high temperature behaviour helps to interpret the compositional transition. The stabilization of the $P2_1/c$ structure at higher temperature in strained crystals parallels that in the Ca-Mg pyroxenes to higher Ca content at room temperature. As such, the

~0.85Å value can be considered the strain-free transition ionic radius for the transition as a function of composition.

The $P2_1/c$-$C2/c$ phase transition and phase equilibria in pigeonite

Ca-poor $P2_1/c$ pigeonite is a high temperature phase, which inverts during cooling to an augite-orthopyroxene assemblage, and it is generally reported as being more iron rich than other pyroxenes. In ternary equilibria between monoclinic Ca-rich, Ca-poor and orthorhombic quadrilateral pyroxenes, the Ca-poor monoclinic pyroxene phase invariably has a lower Mg content (Lindsley and Andersen, 1983).

In Figure 11 we plot the M2 ionic radii of the Ca-poor phase coexisting with Ca-rich clinopyroxene and orthopyroxene at room pressure with the temperature for the ternary equilibria (Lindsley, 1983). As temperature increases, the maximum Mg solubility increases too, while the Ca content at the equilibrium does not change significantly, being ~ 0.2 Ca atoms p.f.u. The average ionic radius was calculated from the crystal chemical composition, assuming that all Ca goes in the M2 site. Fe and Mg were partitioned between the M1 and M2 sites at the equilibrium temperature from the thermometric calibration by Pasqual *et al.* (2000).

In the plot in Fig. 11 only pigeonite above the M2 ionic radius-T stability curve is stable as a single phase; at the same temperature a single phase pigeonite with smaller average ionic radius is not stable, and a two pyroxene assemblage is found instead.

In the same plot the transition temperature for a series of TEM characterized single crystals of varying composition is reported. Coupling of Fe-Mg disorder with the displacive process of the transition also changes the transition temperature, and is likely the reason for the non-linear trend in the phase transition temperatures shown in Fig. 11. A HT-*C*2/*c* structure exists above the dashed line. It appears that the limiting equilibrium conditions for the pigeonite stability fall within the HT-*C*2/*c* field, i.e. pigeonite coexisting in equilibrium with clinopyroxene and orthopyroxene has, when it is formed, a HT-*C*2/*c* structure. Thus the equilibrium occurrence of pigeonite is related to the achievement of an HT-C2/c structure. This explains the high temperature nature of pigeonite, and, as Fe lowers the transition temperature, their likeliness as a Fe-richer phase, at least in assemblages with crystallization temperature below 1200°C. Actually, Mg-rich pigeonite in ureilites is related to their higher crystallization temperature, well beyond 1200°C (Berkley *et al.,* 1980).

Incidentally, this agrees with previous observations that the structure of *C*2/*c* Ca-rich pyroxenes at high temperature approaches that of the HT-*C*2/*c* in Ca-poor pyroxene (Cameron and Papike, 1981, Benna *et al.,* 1990,), making solid solution in *C*2/*c* at high temperature easier.

References

Alvaro, M., Nestola, F., Boffa Ballaran, T., Cámara, F., Domeneghetti, M. C., and Tazzoli, V. (2010) High-pressure phase transition of a natural pigeonite. *American Mineralogist*, **95**, 300-311

Alvaro, M., Cámara, F., Domeneghetti, M.C., Nestola, F., and Tazzoli, V. (2011) HT $P2_1/c$–$C2/c$ phase transition and kinetics of Fe^{2+}–Mg order–disorder of an Fe-poor pigeonite: implications for the cooling history of ureilites. *Contributions to Mineralogy and Petrology*, **162**, 599-613

Arlt, T., and Angel, R.J. (2000) Displacive phase transitions in C-centred clinopyroxenes: Spodumene, $LiScSi_2O_6$ and $ZnSiO_3$. *Physics and Chemistry of Minerals*, **27**, 719–731

Belokoneva, E.L., Khisina, N.R., Petushkova, L.V., and Belov, N.V. (1981) X-ray structural analysis of two-phase clinopyroxene from Luna-24 regolith. In Soviet Physics Doklady (Vol. 26, p. 455).

Benna, P., Tribaudino, M., Zanini, G., and Bruno, E. (1990) The crystal structure of $Ca_{0.8}Mg_{1.2}Si_2O_6$ clinopyroxene ($Di_{80}En_{20}$) at T = -130°, 25°, 400° and 700° C. *Zeitschrift für Kristallographie*, **192**, 183-200.

Berkley J.L., Taylor G.J., Keil K., Prinz M. (1980) The nature and origin of ureilites.
Geochimica et Cosmochimica Acta , **44**, 1579-1597

Boyd, F.R., and Schairer, J.F. (1964) The System $MgSiO_3$—$CaMgSi_2O_6$. *Journal of Petrology*, **5**, 275-309.

Brown, G.E., Prewitt, C.T., Papike, J.J., and Sueno, S. (1972) A comparison of the structures of low and high pigeonite. *Journal of Geophysical Research*, **77**, 5778-5789.

Bruno, E., Carbonin, S., and Molin, G. (1982) Crystal structures of Ca-rich clinopyroxenes on the $CaMgSi_2O_6$-$Mg_2Si_2O_6$ join. *Tschermaks Mineralogische und Petrographische Mitteilungen,* **29**, 223-240.

Burnham, C.W. (1967) Ferrosilite. *Carnegie Inst. Wash. Year Book*, **65**, 285-29

Camara, F., Carpenter, M.A., Domeneghetti, M.C., and Tazzoli, V. (2003) Coupling between non-convergent ordering and transition temperature in the $C2/c \leftrightarrow P2_1/c$ phase transition in pigeonite *American Mineralogist*, **88**, 1115-1128

Cameron, M., and Papike, J.J. (1981) Structural and chemical variations in pyroxenes. *American Mineralogist*, **66**, 1-50.

Cameron, M., Sueno, S., Prewitt, C.T., and Papike, J.J. (1973) High-temperature crystal chemistry of acmite, diopside, hedenbergite, jadeite, spodumene, and ureyite. *American Mineralogist*, **58**, 594–618.

Clark, J. R., Ross, M., and Appleman, D.E. (1971) Crystal chemistry of a lunar pigeonite. *American Mineralogist*, **56**, 888-908.

Downs, R.T. (2003) Topology of the pyroxenes as a function of temperature, pressure, and composition as determined from the procrystal electron density. *American Mineralogist*, **88**, 556-566.

Farrugia, L.J. (1999) WinGX suite for small-molecule single-crystal crystallography. *Journal of Applied Crystallography*, **32**, 837–838.

Frey, F., Weidner, E., Pedersen, B., Boysen, H., Burghammer, M., and Hoelzel, M. (2010) Pyroxene from martian meteorite NWA856: Structural investigations by X-ray and neutron diffraction. *Zeitschrift für Kristallographie*, **225**, 287-297.

Ghose, S., Wan, C., and Okamura, F. (1987) Crystal-structures of $CaNiSi_2O_6$ and $CaCoSi_2O_6$ and some crystal-chemical relations in *C*2/*c* clinopyroxenes. *American Mineralogist*, **72**, 375–381.

Gori, C., Tribaudino, M., Mantovani, L., Delmonte, D., Mezzadri, F., Gilioli, E., and Calestani, G. (2015) Ca-Zn solid solutions in *C*2/*c* pyroxenes: synthesis, crystal structure, and implications for Zn geochemistry. *American Mineralogist*,**100**, 2209-2218.

Lindsley, D.H. (1983) Pyroxene thermometry. *American Mineralogist*, **68**, 477–493.

Lindsley, D.H., and Andersen, D.J. (1983) A two-pyroxene thermometer. *Journal of Geophysical Research: Solid Earth*, **88**, 887-906.

Lufaso, M.W., and Woodward, P.M. (2004) Jahn–Teller distortions, cation ordering and octahedral tilting in perovskites. *Acta Crystallographica Section B: Structural Science*, 60, 10-20.

Mantovani, L., Tribaudino, M., Mezzadri, F., Calestani, G., and Bromiley, G. (2013) The structure of (Ca, Co)$CoSi_2O_6$ pyroxenes and the Ca-M^{2+} substitution in (Ca, M^{2+}) M^{2+} Si_2O_6 pyroxenes (M^{2+}= Co, Fe, Mg). *American Mineralogist*,**98**, 1241-1252.

Mantovani, L., Tribaudino, M., Bertoni, G., Salviati, G., and Bromiley, G. (2014) Solid solutions and phase transitions in (Ca, M^{2+}) M^{2+} Si_2O_6 pyroxenes (M^{2+}= Co, Fe, Mg). *American Mineralogist*, **99**, 704-711.

Momma, K. and Izumi, F. (2008) VESTA: a three-dimensional visualization system for electronic and structural analysis. *Journal of Applied Crystallography*, **41**, 653-658.

Morimoto, N., and Güven, N. (1970) Refinement of the crystal structure of pigeonite. *American Mineralogist*, **55**, 1195-1209.

Nestola, F., Tribaudino, M., and Boffa Ballaran, T. (2004) High pressure behavior, transformation and crystal structure of synthetic iron-free pigeonite. *American Mineralogist*, **89**, 189-196.

Ohashi, Y. (1984) Polysynthetically-twinned structures of enstatite and wollastonite. *Physics and Chemistry of Minerals*, **10**, 217-229.

Ohashi, Y., and Finger, L.W. (1973) Lunar pigeonite crystal structure of primitive-cell domains. *American Mineralogist*, **58**, 1106-1116.

Ohashi, Y., and Finger, L.W. (1976) The effect of Ca substitution on the structure of clinoenstatite. *Year Book - Carnegie Institution of Washington*, **75**, 743-746.

Ohashi, Y., Burnham, C.W., and Finger, L.W. (1975) The effect of Ca-Fe substitution on the clinopyroxene crystal structure. *American Mineralogist*, **60**, 423–434

Pannhorst, W. (1984) High temperature crystal structure refinements of low-clinoenstatite up to 700 °C. *Neues Jahrbuch für Mineralogie Abhandlungen*, **150**, 219–228

Pasqual, D., Molin, G., and Tribaudino, M. (2000) Single-crystal thermometric calibration of Fe-Mg order-disorder in pigeonites. *American Mineralogist*, **85**, 953-962.

Redhammer, G. J. and Roth G. (2004) Structural variation and crystal chemistry of LiMe^{3+} Si_2O_6 clinopyroxenes Me^{3+}= Al, Ga, Cr, V, Fe, Sc and In. *Zeitschrift für Kristallographie-Crystalline Materials,* **219**, 278-294.

Redhammer, G. J., Cámara, F., Alvaro, M., Nestola, F., Tippelt, G., Prinz, S, Simons J, Roth G. and Amthauer, G. (2010). Thermal expansion and high-temperature P21/c–C2/c phase transition in clinopyroxene-type LiFeGe2O6 and comparison to NaFe (Si, Ge)$_2O_6$. *Physics and Chemistry of Minerals*, **37**, 685-704.

Robinson, K., Gibbs, G.V., and Ribbe, P.H. (1971) Quadratic elongation: A quantitative measure of distortion in coordination polyhedra. *Science*, **172**, 567–570.

Sheldrick, G.M. (1996) SADABS. University of Göttingen, Germany.

Sheldrick, G. M. (2009) TWINABS. University of Göttingen, Germany.

Sheldrick, G.M. (1997) SHELXL-97, program for crystal structure solution. University of Göttingen, Germany.

Sheldrick, G. M. (2008) A short history of SHELX. *Acta Crystallographica Section A: Foundations of Crystallography,* **64,** 112-122.

Shimobayashi, N., and Kitamura, M. (1991) Phase transition in Ca-poor clinopyroxenes: a high temperature transmission electron microscopic study. *Physics and Chemistry of Minerals*, **18**, 153–160.

Takeda, H. (1972) Structural studies of rim augite and core pigeonite from lunar rock 12052. *Earth and Planetary Science Letters,* **15**, 65-71.

Takeda, H. (1987) Mineralogy of Antarctic ureilites and a working hypothesis for their origin and evolution. *Earth and Planetary Science Letters*, **81**, 358-370.

Tribaudino, M. (2000) A transmission electron microscope investigation of the $C2/c \rightarrow P2_1/c$ phase transition in clinopyroxenes. *American Mineralogist*, **85**, 707-715.

Tribaudino, M., and Nestola, F. (2002) Average and local structure in $P2_1/c$ pyroxenes along the join diopside-enstatite ($CaMgSi_2O_6$-$Mg_2Si_2O_6$). *European Journal of Mineralogy*, **14**, 549-555.

Tribaudino, M. (2006) Microtextures and crystal chemistry of pigeonite in the ureilites ALHA77257, RKPA80239, Y-791538, and ALHA81101. *Meteoritics and Planetary Science*, **41**, 979-988.

Tribaudino, M., Benna, P., and Bruno, E. (1989) Average structure and M2 site configurations in $C2/c$ clinopyroxenes along the Di-En join. *Contributions to Mineralogy and Petrology*, **103**, 452–456.

Tribaudino, M., Nestola, F., Cámara, F., and Domeneghetti, M.C. (2002) The high-temperature $P2_1/c$-$C2/c$ phase transition in Fe-free pyroxene ($Ca_{0.15}Mg_{1.85}Si_2O_6$): structural and thermodynamic behavior. *American Mineralogist*, **87**, 648–657.

Tribaudino, M., Pasqual, D., Molin, G., and Secco, L. (2003) Microtextures and crystal chemistry in $P2_1/c$ pigeonites. *Mineralogy and Petrology*, **77**, 161-176.

Tribaudino, M., Mantovani, L., Bersani, D., and Lottici, P.P. (2012) Raman spectroscopy of (Ca,Mg)$MgSi_2O_6$ clinopyroxenes. *American Mineralogist*, **97**, 1339-1347.

Weinbruch, S., Styrsa, V., and Müller, W.F. (2003) Exsolution and coarsening in iron-free clinopyroxene during isothermal annealing. *Geochimica et Cosmochimica Acta*, **67**, 5071-5082

Zhang J.S, Reynard B., Montagnac G., Bass J. (2013) Pressure-induced *Pbca*-$P2_1/c$ phase transition of natural orthoenstatite: compositional effect and its geophysical implications. *American Mineralogist*, **98**, 986-992

Zhang J.S, Reynard B., Montagnac G., Bass J. (2014) Pressure-induced *Pbca*–$P2_1/c$ phase transition of natural orthoenstatite: The effect of high temperature and its geophysical implications. *Physics of the Earth and Planetary Interiors*, **228**, 150–159

Table 1: cell parameters and main structural results of pigeonite samples

	$(Ca_{0.2}Co_{0.8})CoSi_2O_6$	ALHA77257	RPKA80239
a (Å)	9.719(2)	9.675(2)	9.675(2)
b (Å)	8.955(3)	8.869(3)	8.882(3)
c (Å)	5.242(1)	5.217(1)	5.212(1)
β (°)	108.43(1)	108.47(2)	108.50(2)
V (Å3)	432.8(2)	424.6(2)	424.8(2)
Space group	$P2_1/c$	$P2_1/c$	$P2_1/c$
Z	4	4	4
Range of hkl	$-14 \leq h \leq 13$, $0 \leq k \leq 13$, $0 \leq l \leq 7$	$-1 \leq h \leq 13$, $-12 \leq k \leq 12$, $-7 \leq l \leq 7$	$-1 \leq h \leq 13$, $-12 \leq k \leq 12$, $-7 \leq l \leq 7$
Radiation	Mokα	Mokα	Mokα
No. of indep. refl. $I > 2\sigma$	1404	1236	1236
2θmax (°)	64°	60°	60°
R_{int} (%)	-	7.99	6.95
R_{all} (%)	11.6	6.4	8.8
R_1 (%)	6.44	4.20	6.07
No. parameters	91	96	95
Goof	1.039	1.063	1.136

Weighted full-matrix least square anisotropic refinements were completed using SHELXL-97 $w=1/[\sigma^2(F_o^2)+(a*P)^2+(b*P)]$ where $P=(F_o^2+2F_c^2)/3$ (Sheldrick, 1997).

Table 2: fractional coordinates and displacement parameters of pigeonite samples

		$(Ca_{0.2}Co_{0.8})CoSi_2O_6$	**ALHA77257**	**RPKA80239**
M2				
	x	0.2543(1)	0.2559(1)	0.2557(1)
	y	0.0142(1)	0.0179(1)	0.0183(1)
	z	0.2255(2)	0.2230(2)	0.2239(3)
	U_{eq}	0.0153(3)	0.0115(3)	0.0145(4)
M1				
	x	0.2509(1)	0.2508(1)	0.2507(2)
	y	0.6546(1)	0.6539(1)	0.6538(2)
	z	0.2311(2)	0.2244(2)	0.2252(3)
	U_{eq}	0.0098(2)	0.0064(3)	0.0097(4)
TA				
	x	0.0431(2)	0.0425(1)	0.0430(2)
	y	0.3403(2)	0.3409(1)	0.3411(2)
	z	0.2789(4)	0.2844(2)	0.2844(3)
	U_{eq}	0.0086(4)	0.0052(2)	0.0096(4)
TB				
	x	0.5508(2)	0.5506(1)	0.5506(2)
	y	0.8367(2)	0.8377(1)	0.8375(1)
	z	0.2397(4)	0.2336(2)	0.2351(3)
	U_{eq}	0.0093(4)	0.0054(2)	0.0095(4)
O1A				
	x	0.8676(5)	0.8666(3)	0.8665(4)
	y	0.3385(5)	0.3391(3)	0.3382(4)
	z	0.1738(9)	0.1758(5)	0.1769(7)
	U_{eq}	0.0098(9)	0.0070(5)	0.0108(7)
O2A				
	x	0.1191(6)	0.1214(3)	0.1217(4)
	y	0.5004(6)	0.5013(3)	0.5011(4)
	z	0.332(1)	0.3239(5)	0.3270(8)
	U_{eq}	0.012(1)	0.0080(5)	0.0113(7)
O3A				
	x	0.1041(6)	0.1057(3)	0.1063(4)
	y	0.2623(6)	0.2726(3)	0.2714(4)
	z	0.578(1)	0.5979(5)	0.5977(8)
	U_{eq}	0.018(1)	0.0106(5)	0.0147(8)
O1B				
	x	0.3750(5)	0.3739(3)	0.3740(4)
	y	0.8381(5)	0.8386(2)	0.8384(4)
	z	0.138(1)	0.1287(5)	0.1283(7)
	U_{eq}	0.0105(1)	0.0073(5)	0.0092(7)
O2B				
	x	0.6288(6)	0.6310(3)	0.6310(4)
	y	0.9860(6)	0.9862(3)	0.9866(4)
	z	0.374(1)	0.3797(5)	0.3782(8)
	U_{eq}	0.019(1)	0.0110(5)	0.0157(8)
O3B				
	x	0.6046(5)	0.6049(3)	0.6042(4)
	y	0.7077(6)	0.7023(3)	0.7022(4)
	z	0.480(1)	0.4669(5)	0.4680(7)
	U_{eq}	0.013(1)	0.0096(5)	0.0133(8)

Table 3: selected bond length (Å) and angles (°) of pigeonite samples.

	$(Ca_{0.2}Co_{0.8})CoSi_2O_6$	**ALHA77257**	**RPKA80239**
M2-O1A	2.134(5)	2.144(2)	2.148(4)
M2-O2A	2.069(5)	2.084(4)	2.071(4)
M2-O3A	2.454(6)	2.321(4)	2.325(5)
M2-O1B	2.100(5)	2.105(2)	2.115(5)
M2-O2B	2.045(5)	2.014(3)	2.015(4)
M2-O3B	3.020(6)	3.034(4)	3.032(5)
<M2-O> 6 atoms	2.304	2.284	2.284
V_{M2}(Å^3) 6 atoms	11.11	10.97	10.95
OQE_{M2}	1.320	1.309	1.311
OAV_{M2}	510.04	620.7	514.37
M2-O3A	3.492(6)	3.583(3)	3.567(4)
M2-O3B	2.642(5)	2.513(2)	2.523(4)
<M2-O> 8 atoms	2.495	2.475	2.475
V_{M2}(Å^3) 8 atoms	23.27	22.68	22.70
M1-O1A	2.072(5)	2.037(2)	2.043(4)
M1-O1A	2.156(5)	2.153(3)	2.143(5)
M1-O2A	2.064(5)	2.020(4)	2.025(4)
M1-O1B	2.093(6)	2.069(2)	2.062(5)
M1-O1B	2.182(5)	2.174(3)	2.179(4)
M1-O2B	2.089(6)	2.052(2)	2.049(5)
<M1-O>	2.109	2.084	2.084
V_{M1}(Å^3)	12.38	11.94	11.92
OQE_{M1}	1.007	1.008	1.008
OAV_{M1}	22.44	25.09	24.36
TA-O1A	1.614(6)	1.614(2)	1.620(4)
TA-O2A	1.596(5)	1.596(3)	1.594(4)
TA-O3A	1.647(5)	1.647(2)	1.643(4)
TA-O3A	1.632(5)	1.668(3)	1.671(5)
<TA-O>	1.626	1.641	1.639
V_{TA}(Å^3)	2.186	2.250	2.245
TQE_{TA}	1.006	1.008	1.008
TAV_{TA}	25.15	32.98	34.78
TA-O1B	1.621(6)	1.622(3)	1.620(4)
TA-O2B	1.588(5)	1.595(2)	1.596(4)
TA-O3B	1.651(5)	1.672(2)	1.670(4)
TA-O3B	1.668(6)	1.673(3)	1.670(4)
<TB-O>	1.632	1.631	1.632
V_{TB}(Å^3)	2.219	2.205	2.020
TQE_{TB}	1.004	1.004	1.004
TAV_{TB}	15.67	18.96	18.52
O3A-O3A-O3A	189.6(3)	197.5(1)	196.6(2)
O3B-O3B-O3B	147.8(2)	144.0(1)	143.9(2)
O3A-T-O3A	138.9(2)	135.4(1)	135.5(1)
O3B-T-O3B	133.2(2)	130.4(1)	130.6(1)

TQE, TAV, OQE and OAV are quadratic elongation and angle variance for tetrahedra and octahedra (Robinson *et al.,*. 1971). The values for the kinking angles O3-O3-O3 and O3-T-O3 linkage are calculate with VESTA (Momma and Izumi, 2008).

Table 4: anisotropic displacement parameters for the single crystal **$(Ca_{0.2}Co_{0.8})CoSi_2O_6$**

	U_{11}	U_{22}	U_{33}	U_{23}	U_{13}	U_{12}
CoM1	0.0093(4)	0.0114(5)	0.0097(5)	0.0010(4)	0.0047(3)	0.0002(4)
CaM2	0.0131(5)	0.0208(6)	0.0121(5)	0.0025(4)	0.0041(4)	0.0021(5)
CoM2	0.0131(5)	0.0208(6)	0.0121(5)	0.0025(4)	0.0041(4)	0.0021(5)
TA	0.0073(9)	0.0080(9)	0.0106(9)	-0.0009(7)	0.0032(7)	-0.0007(7)
O1A	0.010(2)	0.010(2)	0.009(2)	0.0025(18)	0.0025(18)	0.0021(19)
O2A	0.014(3)	0.011(2)	0.015(3)	0.0002(19)	0.007(2)	-0.004(2)
O3A	0.006(2)	0.028(3)	0.021(3)	0.012(2)	0.004(2)	0.0001(2)
TB	0.0098(9)	0.0096(9)	0.0098(9)	-0.0011(7)	0.0047(7)	-0.0005(7)
O1B	0.009(2)	0.009(2)	0.013(2)	-0.0001(18)	0.0044(18)	-0.0001(19)
O2B	0.019(3)	0.014(3)	0.033(3)	0.004 (2)	0.019(3)	-0.006(2)
O3B	0.009(2)	0.019(3)	0.013(2)	0.0054(19)	0.002(2)	-0.001(2)

Captions of the Figures

Figure 1: comparison of the structures of *C*2/*c* $(Ca_{0.4}Co_{0.6})CoSi_2O_6$ and *P*2_1/*c* $(Ca_{0.2}Co_{0.8})CoSi_2O_6$ (Mantovani *et al.,*. 2013, this work). The two structure are projected onto (100). Bond lengths and kinking angles are shown.

Figure 2: a) M2-O, b), M1-O, c) individual and d) average T-O bond lengths of Ca-Co pyroxenes *vs* Ca content. Data for Ca-Co: Mantovani *et al.* (2013), this work.

Figure 3: tetrahedral structural parameters in Ca-Co pyroxenes a) difference between average bond length T-O bridging and non-bridging oxygen; b) T-O-T and O3-O3-O3 angle; c) bond angle variance of the M1 octahedron and the T tetrahedron in Ca-Co pyroxenes. Data for Ca-Co: Mantovani *et al.* (2013), this work.

Figure 4: displacement parameters in $Ca_{0.20}Co_{1.80}Si_2O_6$, $Ca_{0.15}Mg_{1.85}Si_2O_6$ and $Mg_2Si_2O_6$ *P*2_1/c pyroxenes (this work; Tribaudino *et al.,*. 2002; Pannhorst, 1984)

Figure 5. Major axis of the atomic displacement parameter ellipsoid for oxygen in Ca-Mg pyroxenes and in $Ca_{0.2}Co_{1.8}Si_2O_6$. The three oxygens with higher displacement are in the order O3a, O2b and O3b, in $Ca_{0.2}Co_{1.8}Si_2O_6$ and $Ca_{0.23}Mg_{1.77}Si_2O_6$.

Figure 6: O3-O3-O3 kinking angle of synthetic Ca-Mg, Ca-Fe and Ca-Co pyroxenes and natural pigeonites *vs* average M2 ionic radius. . Data from: Ca-Mg: Ohashi and Finger (1976), Bruno *et al.*. (1982), Tribaudino *et al.* (1989), Tribaudino and Nestola (2002), Tribaudino *et al.* (2012); Ca-Fe: Burnham (1967), Ohashi *et al.* (1975); Ca-Co: Mantovani *et al.* (2013), this work; natural pigeonite: Morimoto and Guven (1970), Clark *et al.*. (1971), Takeda (1972), Brown *et al.* (1972), Ohashi and Finger (1973), Belokoneva *et al.* (1981), Pasqual *et al.* (2000), Camara *et al.* (2003) (also disordered pyroxenes), Tribaudino (2006), Frey *et al.* (2010).

Fig. 7: M2-O3 a) longer and b) shorter distance, c) M2-O2, d) M2-O1 bond distance of synthetic Ca-Mg, Ca-Fe and Ca-Co pyroxenes and of natural pigeonites *vs* average M2 ionic radius. Data as in Fig. 6.

Figure 8 Average M1-O bond distance of synthetic Ca-Mg, Ca-Fe and Ca-Co pyroxenes and natural pigeonites *vs* average M2 ionic radius. Data as in Fig. 6.

Figure 9: Difference between average bond length T-O bridging and non-bridging of synthetic Ca-Mg, Ca-Fe, Ca-Co and Ca-Zn pyroxenes and natural pigeonites *vs* average M2 ionic radius. Data as in Fig. 6, Gori *et al.* (2015) for Ca-Zn pyroxenes.

Figure 10: Longest M2-O3A distance *vs* difference in the O3-O3-O3 kinking angles for synthetic pyroxenes, natural pigeonites, at room and high pressure-temperature conditions. Data from: room conditions, see Fig. 5; high pressure: Nestola *et al.* (2004), Alvaro *et al.*. (2010); high temperature: Tribaudino *et al.* (2002), Camara *et al.* (2003).

Figure 11: M2 ionic radii of the Ca-poor phase coexisting with Ca-rich clinopyroxene and orthopyroxene at room pressure (full), $C2/c$-$P2_1/c$ transition temperature (dashed) and range of natural pigeonite *vs* ionic radius. Red dots indicate transition temperatures, from Shimobayashi and Kitamura (1991), Tribaudino *et al.* (2002), the arrow indicates the transition range between strained and unstrained crystals), Alvaro *et al.* (2011), Camara *et al.*(2003).

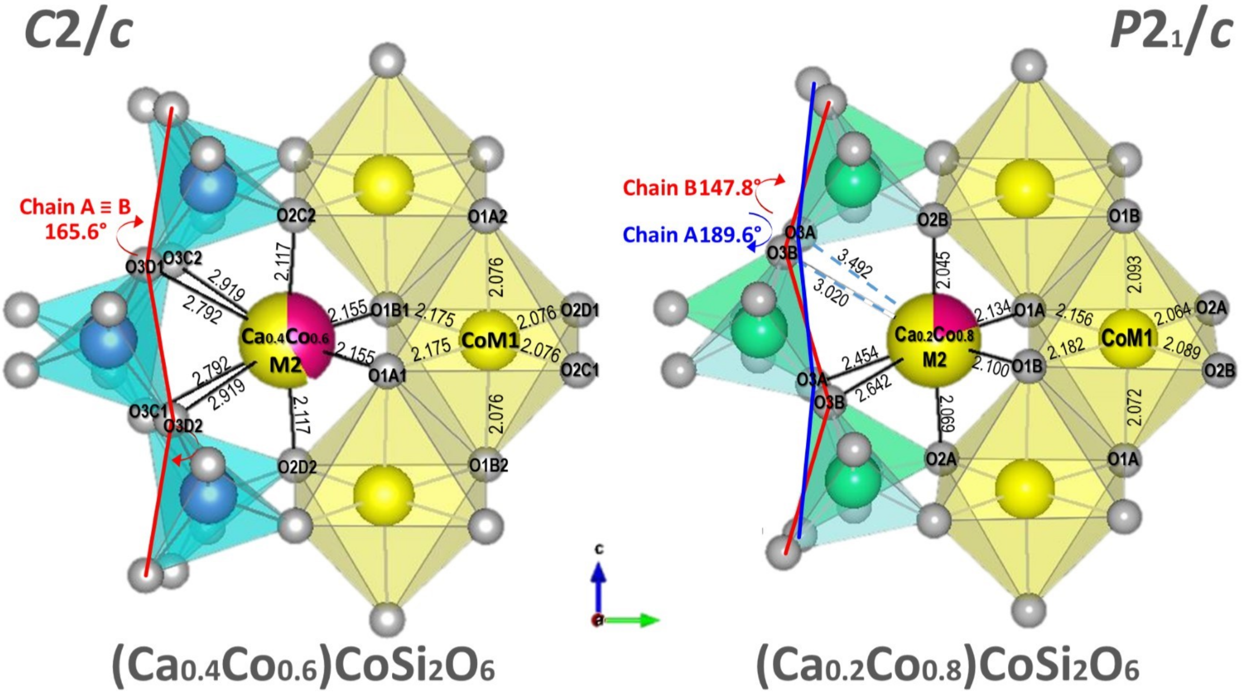

Figure 1: compared structures of $C2/c$ $(Ca_{0.4}Co_{0.6})CoSi_2O_6$ and $P2_1/c$ $(Ca_{0.2}Co_{0.8})CoSi_2O_6$ (Mantovani *et al.,* 2013, this work). The two structure are projected on (100). Bond lengths and kinking angles are shown.

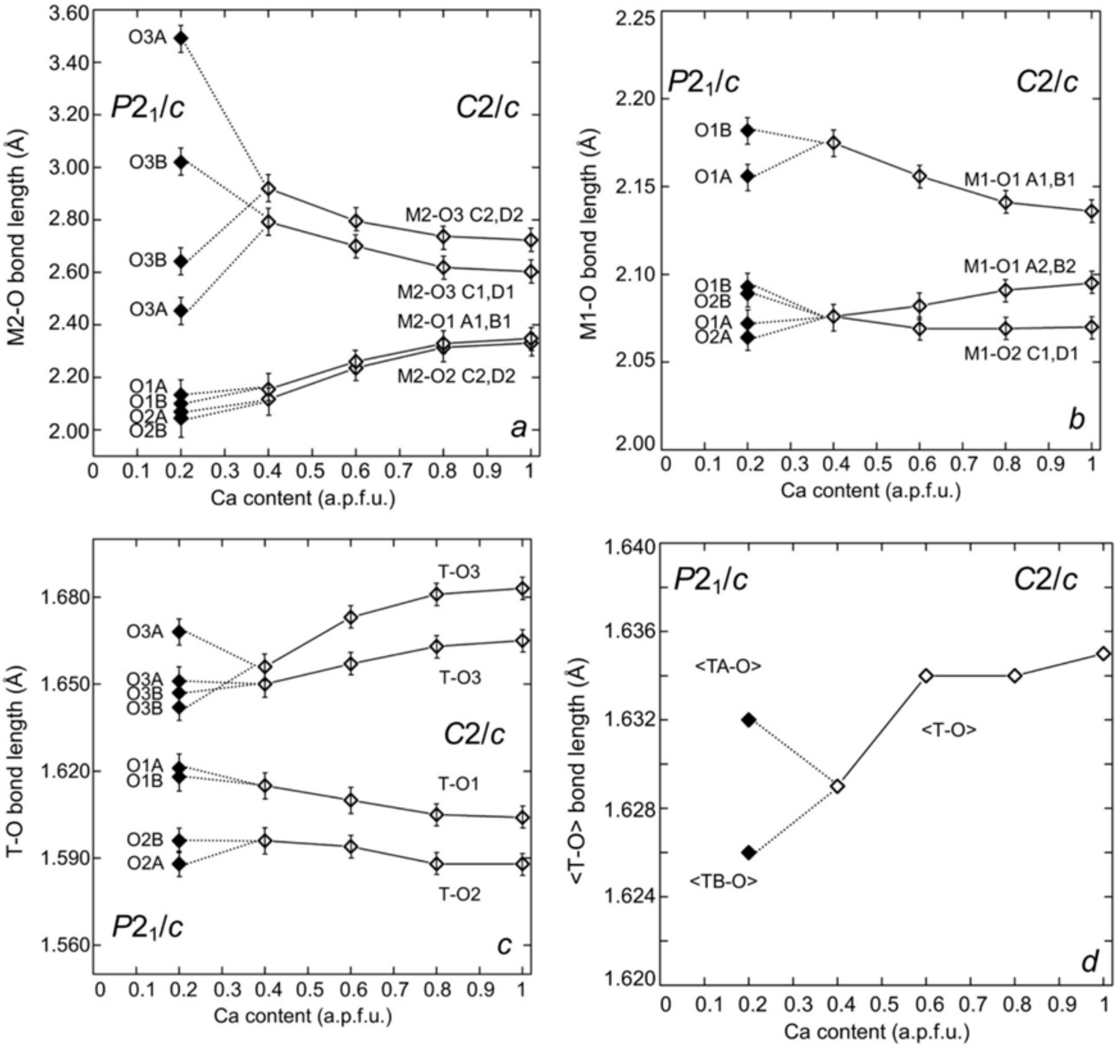

Figure 2: a) M2-O, b), M1-O, c) individual and d) average T-O bond lengths of Ca-Co pyroxenes *vs* Ca content. Data for Ca-Co: Mantovani *et al.,* (2013), this work.

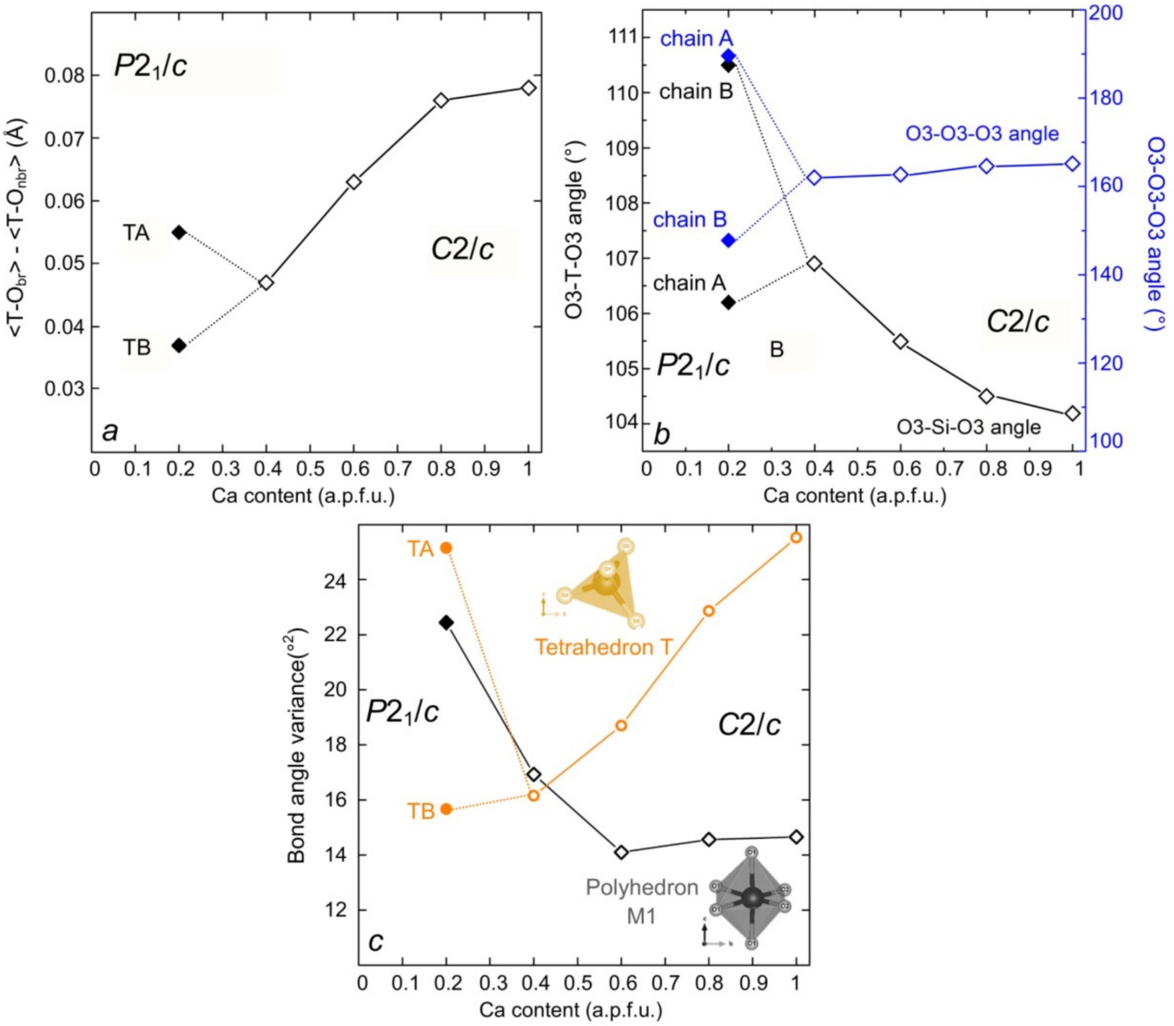

Figure 3: tetrahedral structural parameters in Ca-Co pyroxenes a) difference between average bond length T-O bridging and non-bridging oxygen; b) T-O-T and O3-O3-O3 angle; c) bond angle variance of the M1 octahedron and the T tetrahedron in Ca-Co pyroxenes. Data for Ca-Co: Mantovani *et al.,* (2013), this work.

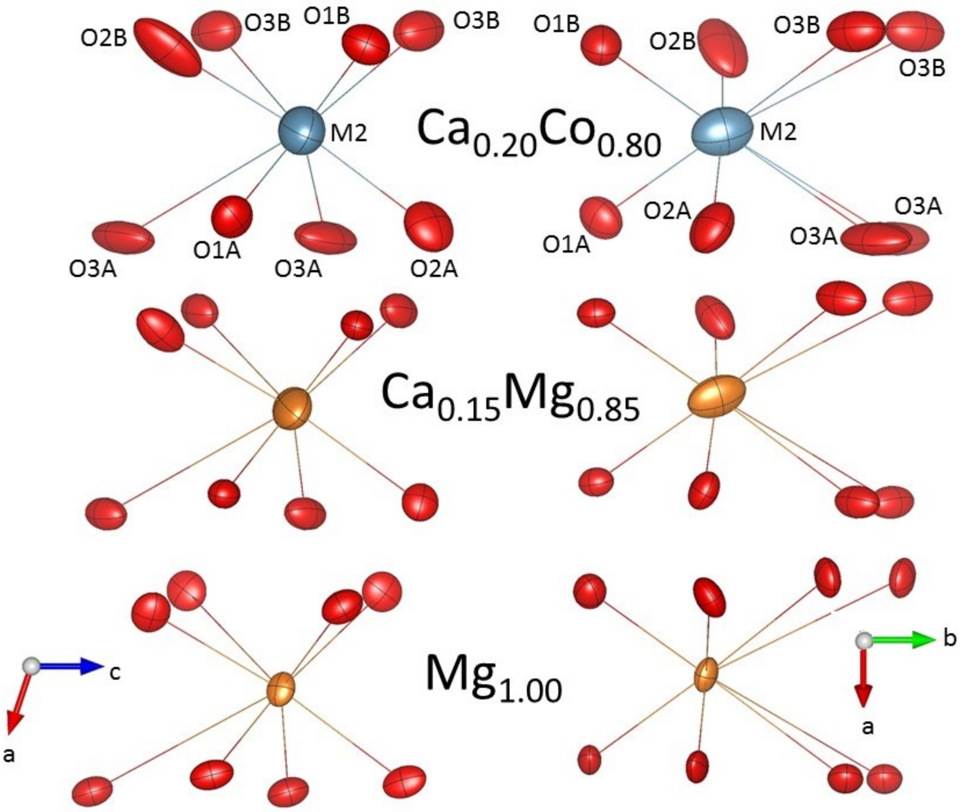

Figure 4: displacement parameters in $Ca_{0.20}Co_{1.80}Si_2O_6$, $Ca_{0.15}Mg_{1.85}Si_2O_6$ and $Mg_2Si_2O_6$ $P2_1/c$ pyroxenes (this work, Tribaudino *et al.,* 2002, Pannhorst 1984)

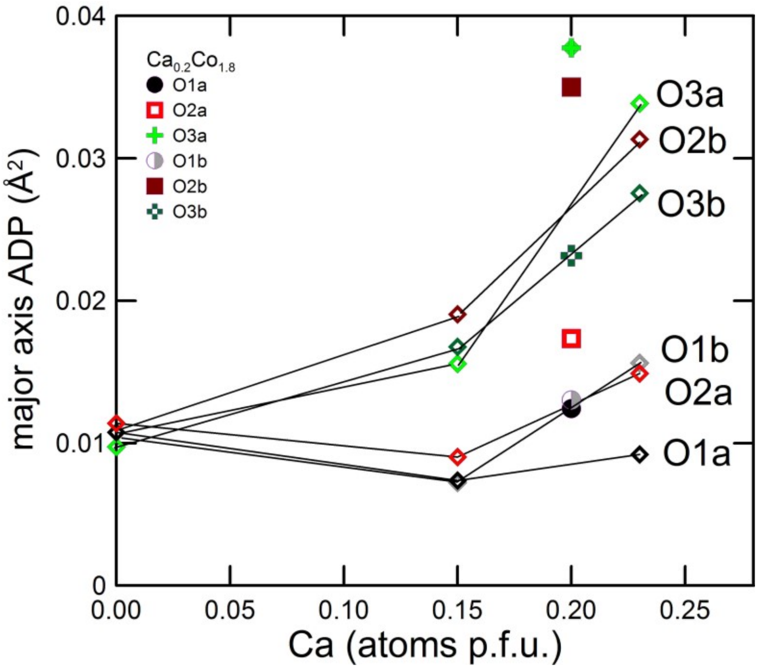

Figure 5. Major axis of the atomic displacement parameter ellipsoid for oxygen in Ca-Mg pyroxenes and in $Ca_{0.2}Co_{1.8}Si_2O_6$. The three most displacement oxygen are in the order O3a, O2b and O3b, in $Ca_{0.2}Co_{1.8}Si_2O_6$ and $Ca_{0.2}Co_{1.8}Si_2O_6$.

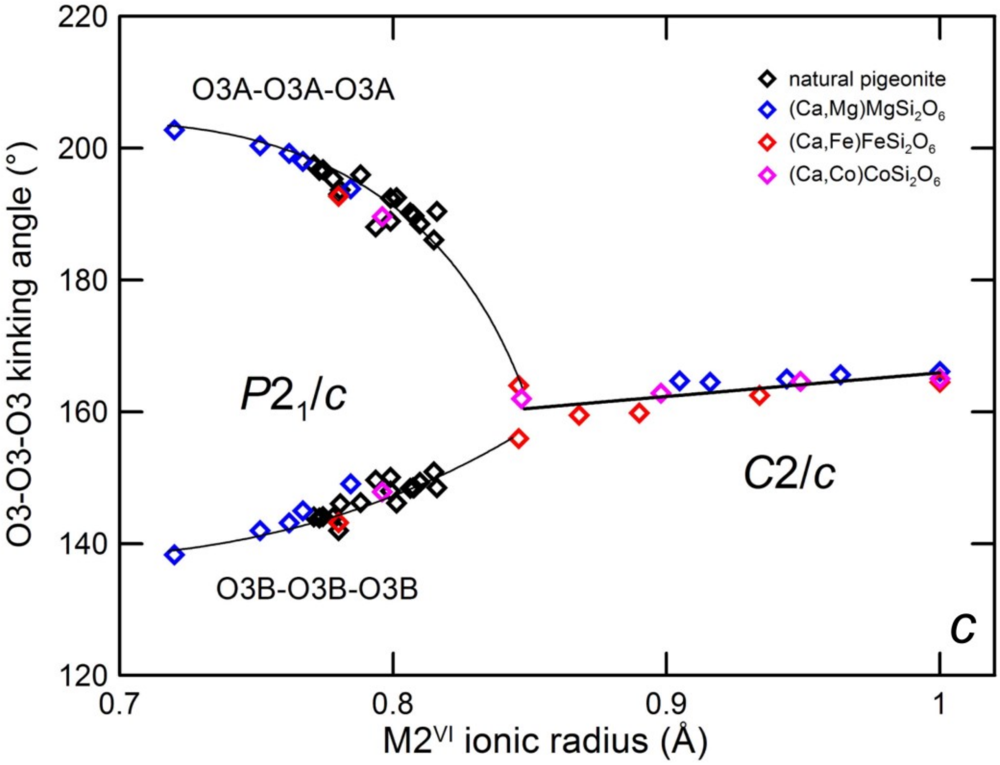

Figure 6: O3-O3-O3 kinking angle of synthetic Ca-Mg, Ca-Fe and Ca-Co pyroxenes and natural pigeonites *vs* average M2 ionic radius. Data from: Ca-Mg: Ohashi and Finger (1976), Bruno *et al.,*. (1982), Tribaudino *et al.,* (1989), Tribaudino and Nestola (2002), Tribaudino *et al.,* (2012); Ca-Fe: Burnham (1967), Ohashi *et al.,* (1975); Ca-Co: Mantovani *et al.,* (2013), this work; natural pigeonite: Morimoto and Guven (1970), Clark *et al.,*. (1971), Takeda (1972), Brown *et al.,* (1972), Ohashi and Finger (1973), Belokoneva *et al.,* (1981), Pasqual *et al.,* (2000), Camara *et al.,* (2003) (also disordered pyroxenes), Tribaudino (2006), Frey *et al.,* (2010).

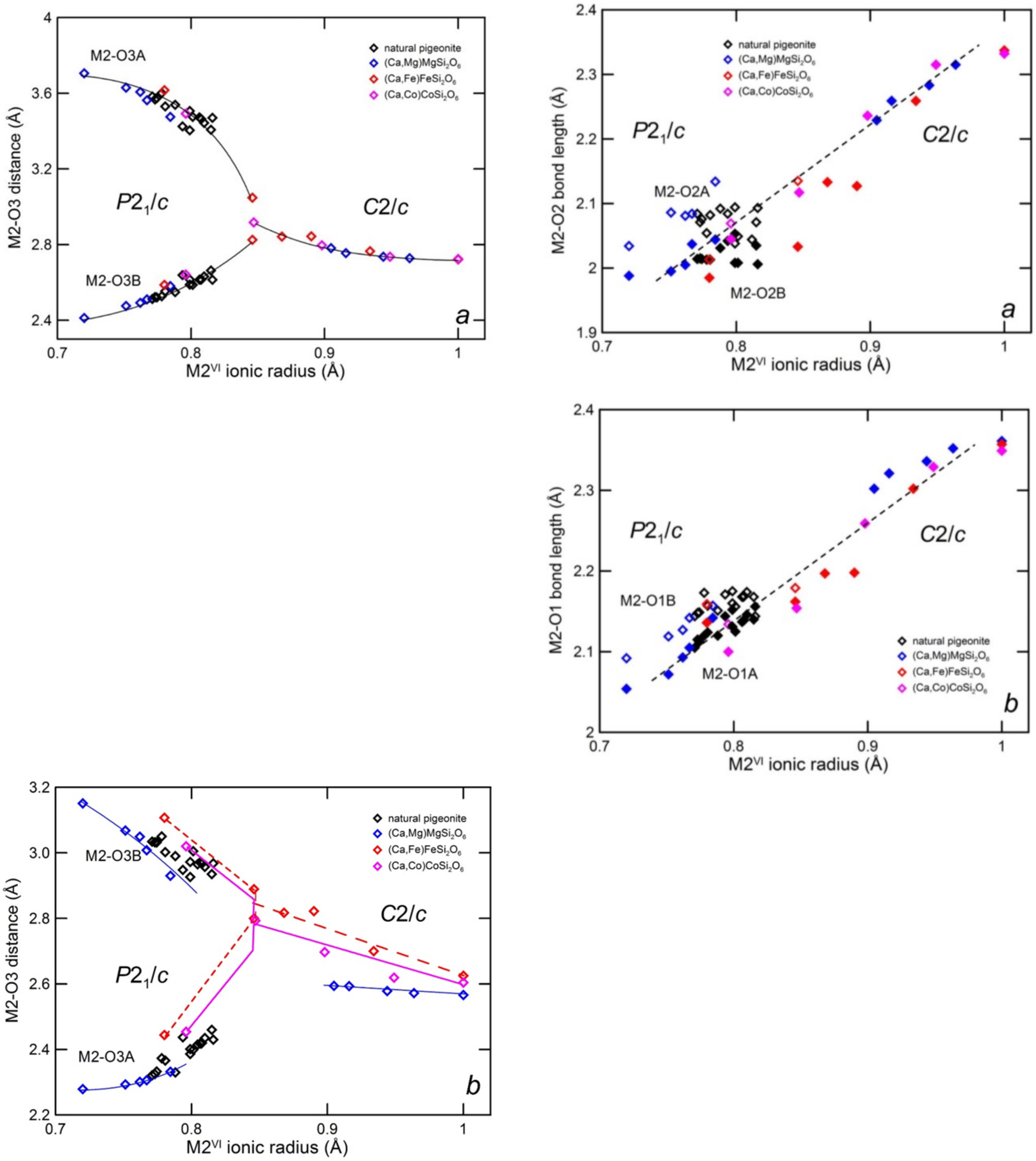

Fig. 7: M2-O3 a) longer and b) shorter distance, c) M2-O2, d) M2-O1 bond distance of synthetic Ca-Mg, Ca-Fe and Ca-Co pyroxenes and of natural pigeonites *vs* average M2 ionic radius. Data as in Fig. 6.

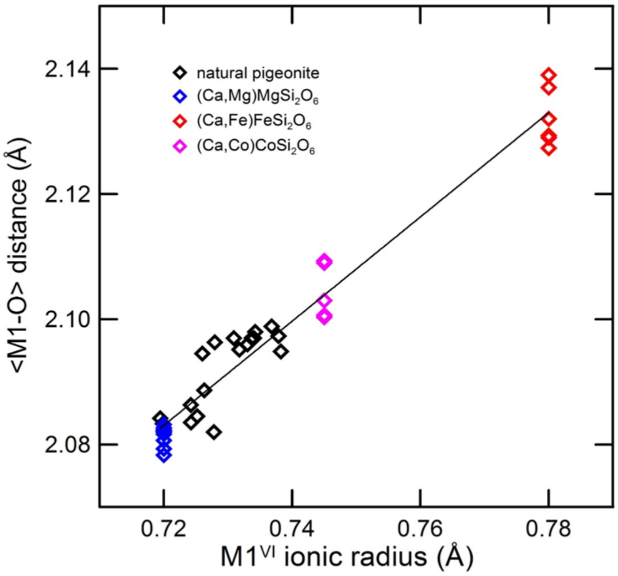

Figure 8: Average M1-O bond distance of synthetic Ca-Mg, Ca-Fe and Ca-Co pyroxenes and natural pigeonites *vs* average M2 ionic radius. Data as in Fig. 6.

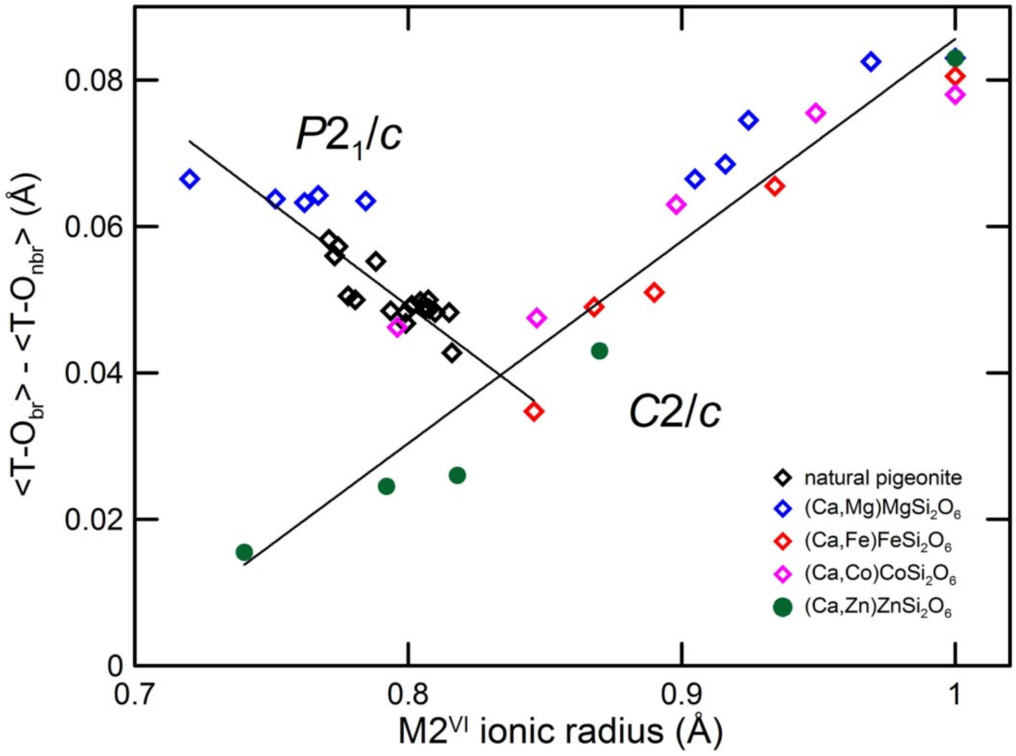

Figure 9: Difference between average bond length T-O bridging and non-bridging of synthetic Ca-Mg, Ca-Fe, Ca-Co and Ca-Zn pyroxenes and natural pigeonites *vs* average M2 ionic radius. Data as in Fig. 5, Gori *et al.,*. (2015) for Ca-Zn pyroxenes.

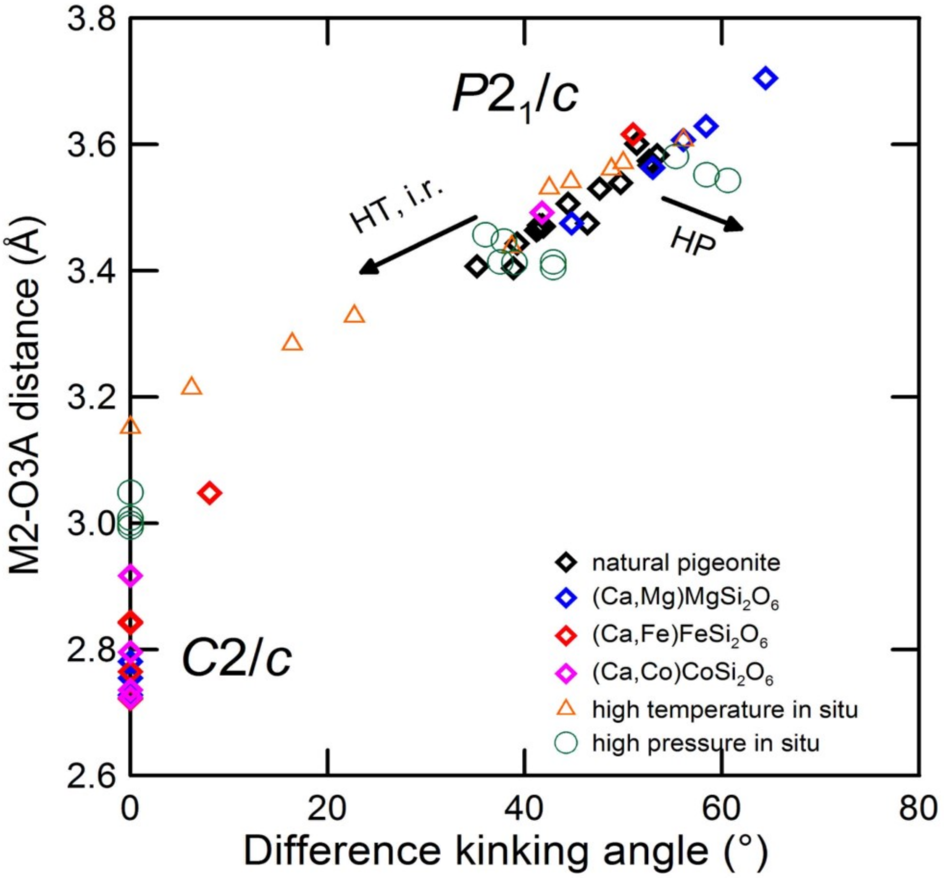

Figure 10: Longest M2-O3A distance *vs* difference in the O3-O3-O3 kinking angles for synthetic pyroxenes, natural pigeonites, at room and high pressure-temperature conditions. Data from: room conditions, Fig. 5; high pressure: Nestola *et al.,* (2004), Alvaro *et al.,*. (2010); high temperature: Tribaudino *et al.,*. (2002), Camara *et al.,* (2003).

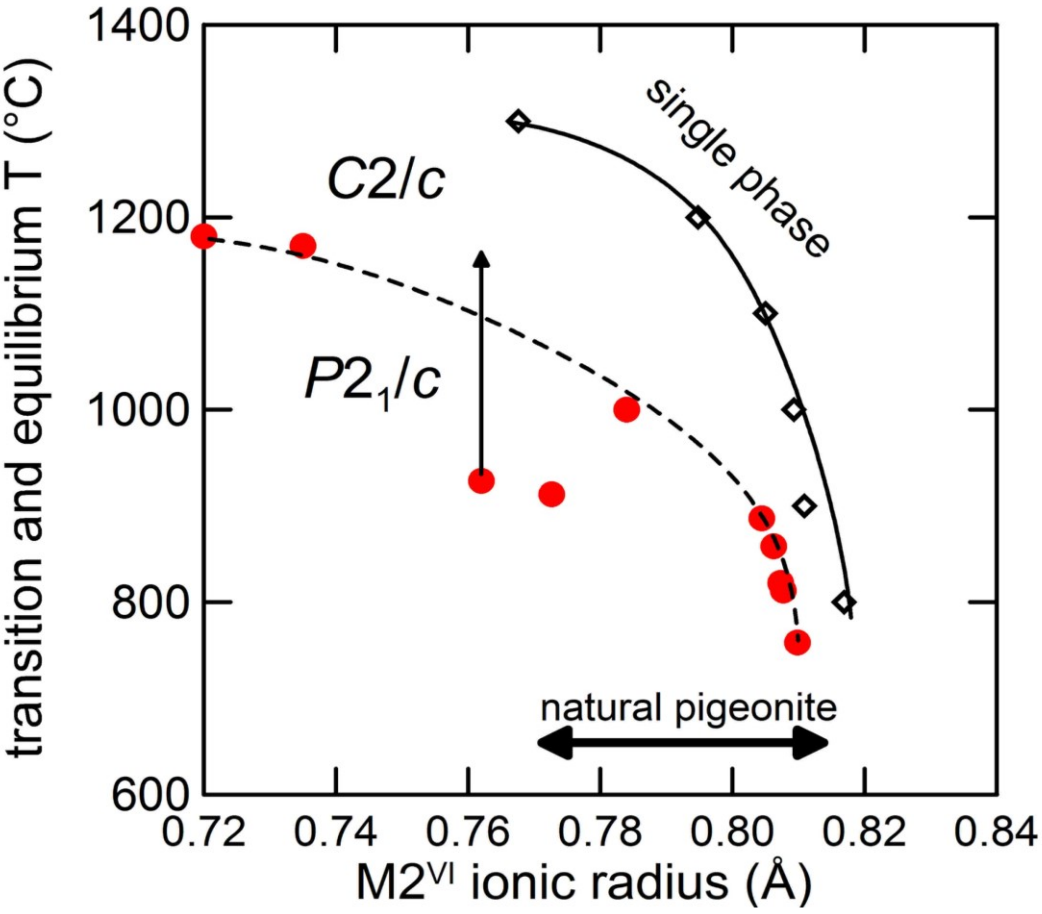

Figure 11: M2 ionic radii of the Ca-poor phase coexisting with Ca-rich clinopyroxene and orthopyroxene at room pressure (full), *C*2/*c*-*P*2$_1$/*c* transition temperature (dashed) and range of natural pigeonite vs ionic radius. Red dots indicate transition temperature, from Shimobayashi and Kitamura (1991), Tribaudino *et al.,*. (2002), the arrow indicates the transition range between strained and unstrained crystals, Alvaro *et al.,*. (2011), Camara *et al.,*. (2003).